Computer vision-based measurement of stormwater discharge: proof-of-concept

Mohammad N. Motlagh[1*], Sierra Young[2], Kenneth Chapman[3], Evelynn Wilcox[1], François Birgand[1]

1 Department of Biological and Agricultural Engineering, North Carolina State University, Raleigh, NC, USA

2 Department of Civil and Environmental Engineering, Utah State University, Logan, UT, USA

3 Department of Biological Systems Engineering, University of Nebraska-Lincoln, Lincoln, NE, USA

* Corresponding author

Email: mnooshz@ncsu.edu

Abstract

Stormwater systems, as infrastructure draining urban water runoff into water bodies, are pivotal in preserving municipal functionality while they play an important hydrological and environmental role. As such, the ability to reliably monitor stormwater outflow in many locations could provide valuable information for water managers. However, in most cases stormwater outlets have not been designed or installed to facilitate the measurement of stormflow, leaving traditional contact-based velocity and water level measurement techniques ill-suited to capture highly variable and turbulent flows. We propose a non-contact alternative approach based on computer vision, capable of quantifying discharge from images and videos obtained from cameras facing the outlets. In variable lighting and on often 'noisy' images and videos, this approach came with its own set of challenges, and classical computer-vision techniques did not perform reliably and accurately. To solve these issues, we used the combination of computer vision and machine learning (CV-ML) techniques, using the round geometry of culverts to our advantage. In our approach, the water stage at the outlet is determined by calculating the difference between the height of the extracted shape of a round culvert and the height of the empty area above water. Then, using a checker board as a reference object, the measurements from images are converted into real-world measurements. Finally, as a first approximation using rating curves, the calculated water stage can be converted into discharge values. To evaluate the model's performance on stage measurements, two methods were considered. In the first, the uncertainty on measurements was assessed by comparing the culvert diameter with that of our CV-ML model calculated value. As a result, the model was on average capable of making measurements within ±1 cm approximately 80% of the times. In the second method, we compared measurements from our model to those 'visually' made from images obtained during a flow event. For this method also the model estimated 63% of the stage values within ±1 cm and 96% within ±2 cm. These results could be considered as satisfactory, especially considering the complexity of the field conditions.

Introduction

Increased urbanization around the world comes with less pervious surfaces and higher peaks of stormwater outflow following rainfall. Detrimental consequences include increased flooding, stream bank erosion, and pollutant loads among many others [1–5]. Many stormwater control measures have been designed and implemented in the field to mitigate stormwater detrimental effects (reviewed by [6]). In urban environments, there are numerous stormwater outlets where installing and maintaining traditional sensors to calculate flow is difficult and expensive. Image-based methods offer the possibility for a more accessible, cost-effective, and possibly more accurate alternative, although it comes with its own challenges.

In hydrology, computer vision has been used for measuring water level and water surface velocity [7–25], and images are being used as an active monitoring tool (e.g., [26, 27]). Image-based measurements are then used to estimate discharge, i.e., the volume of water passed by a point per unit time [28–36]. Image-based methods offer benefits over traditional techniques, including non-contact sensing, access to the velocity field at the surface of the water, access to additional information about environmental conditions, visual verification, access to the 'raw' data, and openness to reanalyzing images using improved algorithms and developments [27, 28, 37–39]. Additionally, the development of communication networks has opened new possibilities to the field, such as the possibility of distant data interpretation or cloud computing [40, 41]. This subsequently obviates the need for field calibration and high-level maintenance at short periodicity, requiring fewer field maintenance visits from high-skill personnel [40].

Traditional machine vision techniques (i.e., not using machine learning) have classically been used to measure water level in relatively calm waters [7, 12, 14, 16, 22, 23, 28, 42–45]. Recently and for example, Chapman et al. (2022) presented details of the GRIME2 water level detection system for small streams [37]. The software's lab results showed an accuracy of ±3 mm (at the USGS standard level) for 80% of the time [46]. Field results, obtained from a tidal marsh in North Carolina, also estimated the accuracy to be within ±3 mm 70% and ±5 mm 90% of the time [27]. Most other studies report values within ±10 mm [9, 40, 47–51].

The measurement of stage is most often used to compute discharge, although this method is not always ideal [52]. In many cases, the velocity of water is also needed to compute discharge. Currently, two categories of methods are used for measuring water surface velocity based on images: motion estimation and feature-point tracking [13]. Additionally, Deep learning models have also been used to measure the velocity of water in coastal areas, based on principles similar to motion estimation methods [18]. Motion estimation methods track changes at the pixel level over short time intervals and include approaches such as optical flow [53], block matching [54], correlation [55], and spatio-temporal orientation [13, 56]. The second category, including the methods of Particle Image Velocimetry (PIV) and Particle Tracking Velocimetry (PTV) as well as their extensions, estimates the displacement of particles in short time intervals and assumes that they have the same velocity as the water [57, 58]. These methods, although useful with streams and storm sewer systems with floating objects, are not fully workable with stormwater outlets. This is due to the difficulties of seeding the water surface and that debris is washed away during the very first moments. In such situations, measuring stage and using a stage-discharge relationship, or employing approximate methods based on stage from open channel flow hydraulics, are a much more viable option, especially given the volatile nature of the flow from the system.

Given the highly variable contextual conditions in field images, deep learning approaches may be a suitable choice for water stage monitoring, compared to classical computer vision techniques. Instead of relying on fixed operations that could impose assumptions (e.g., lighting and contrast conditions) ill-suited to the problem's condition and could fail to adapt accordingly, deep learning models utilize a layered, complex architecture. This approach leverages the versatility from images of the object to develop a better and more generalizable abstraction. Not surprisingly, deep learning approaches have been reported in image-based hydrological monitoring.

Pan et al. (2018) reported on a deep learning system for water level detection and surveillance [40]. The system comprised of three layers: the data acquisition layer, the transmission layer, and the application layer, each containing several modules with four interaction interfaces between layers. The system's performance was compared to two other methods of water level estimation, namely the difference method and the dictionary learning. The results indicated that the deep learning model was more accurate and robust.

Gupta et al. (2022) proposed a ranking system for stream stages based on convolutional neural networks (CNN) [59]. The model was primarily designed for areas lacking observational data and it helped expand the application of image-based stream monitoring by reducing the requirements both for training data and recorded variables. As a result, the model was able to replicate the trends generated by a regression model. Nevertheless, computed discharges were shown to be highly dependent on the distribution of the flows produced by the model.

Stormwater is often routed in circular pipes and culverts, until it is discharged into receiving bodies, i.e., often directly into the receiving streams or ponds. So far, image-based stormwater monitoring methods have mainly used images and videos recorded from inside culverts [13, 35, 47, 60]. However, these areas are typically hard to reach, which makes mounting and maintaining the cameras less practical, if not impossible. Moreover, the presence of hazardous chemicals, as well as the turbulent condition of the water during flow events, could deteriorate cameras' life cycle and impede observation when it is needed. Given these perils, it makes sense to place the camera outside the environment. Conversely, positioning the camera outside the outlet pipes could make the method more practical, given the restrictions in field conditions. Also, because of their circular pattern, culverts and pipes have the potential to be automatically recognized using machine vision approaches. Lastly, the fact that the discharge may, in perched conditions, exhibit a recognizable parabolic free fall pattern from a pipe or culvert could be helpful in calculating the discharge [61].

In this manuscript, we explored the use of a CV-ML approach to automatically measure the water stage at the mouth of stormwater outfall into streams from images taken by inexpensive time lapse cameras. Regarding that, flow rates can first be approximated using the measured stage and a stage-discharge rating curve or Manning's equation. To evaluate the model's performance, we compared the model's ability to measure the diameter of the empty culvert under variable lighting conditions, and, the model's ability to measure water level as compared to measurements performed by the human eye.

Methods

To determine the water level at stormwater outlet round culverts, an instance segmentation model based on the Mask R-CNN architecture was developed [62]. Specifically, the model was trained to detect the empty area delimited by the culvert's boundaries from images where no flow occurred, and also from images when there was water and flow in the pipes based on images captured from the field. Then, by subtracting the height of the empty area from the diameter of the empty culvert, we calculated the water level (Fig 1).

Fig 1. Model capturing an empty outlet (left) and the empty area of the partially filled culvert (right)

In this section, details of the model, including the architecture, dataset, and training configurations are provided. Initially, the concept behind the model is explored through a discussion of the evolution of region-based convolutional neural networks (R-CNN) from their inception to the development of the Mask R-CNN, with the novelty and significance of the model being highlighted. Next, the implementation, including a discussion on the feature extractor and training configurations, was provided. In the final section, details about data collection and annotation, as well as the preprocessing, are presented.

Model architecture

The region-based convolutional neural network (R-CNN) architecture was first introduced as a simple and efficient approach for both object detection and semantic segmentation in images and videos [63]. Its key novelty lies in its simplicity and speed, while also significantly improving object detection accuracy over previous state-of-the-art (SOTA) models. This model works by generating region proposals over the entire image, feeding those regions into a convolutional neural network to extract features corresponding to each region, and then using two fully connected heads, along with dedicated support vector machines, to find the class and the coordinates of the refined region. Lastly, non-maximum suppression is used to remove highly overlapping and duplicate regions, while confidence score thresholding filters out the remaining regions in favor of the desired objects.

Here, region proposals are rectangular areas with a likelihood of containing an object, and features are abstractions generated by the CNN from the provided input. Additionally, 'heads' refer to parts of the architecture from which an output is generated. The term 'fully-connected' refers to the fact that the output is generated by considering the entirety of the input provided to the last stage, as opposed to the 'convolutional' approach, which considers regional data when providing an output. Using fully-connected heads also has mathematical justification given their full matrix representation provides flexibility to obtain the desired dimensions for the output while the banded representation of the convolutional layers is incapable of accommodating such flexibility.

The next generation of this model, called Fast R-CNN, was introduced with substantial improvement in training and inference speed [65]. Unlike R-CNN, which generates region proposals over the original image, Fast R-CNN generated them after the feature extractor, reducing the computational burden for each image to a single pass. This efficiency gain is further amplified by using deeper feature extractors like VGG16 [64], which provide richer features for downstream components, leading to increased accuracy. While deeper features might have increased processing time, the efficiency of processing each image only once offset this cost.

Next, the Faster R-CNN architecture was introduced, which was an improvement upon its predecessors primarily thanks to the incorporation of the Region Proposal Network (RPN) [66]. Unlike previous generations that relied on external tools for generating region proposals, this network has a dedicated component — the RPN — for this task. This allows the RPN to learn and improve through training data and backpropagation, leading to more precise region proposals and, consequently, a more accurate model output. In our case, this corresponds to finding in an otherwise 'busy' image the region where the stormwater culverts are located. Additionally, compared to previous generations, this model introduced significant improvements in both training and inference speed.

The Mask R-CNN model is considered as an extension of the Faster R-CNN architecture, providing SOTA instance segmentation by adding a segmentation head parallel to the classification and object detection heads already present in the Faster R-CNN architecture. Its novelty lies in the introduction of the ROIAlign layer, which employs bilinear interpolation instead of the pooling operation to precisely preserve the locations of region proposal boundaries. Regarding that, the ROI is divided into bins and pixels overlapping each bin are represented by a sample point. Then, the value of each point is computed through a bilinear interpolation from neighboring grid points. This contrasts with the ROIPool layer in Fast R-CNN architecture, which quantizes and aggregates region proposals, typically using max pooling, potentially leading to misalignment. As a result of this innovation, Mask R-CNN has achieved a relative improvement in mask prediction accuracy ranging from 10% to 50% [62]. In our case, this would apply on the ability on the model to find the empty area inside a culvert.

Given the complexity of real-world image data and the turbulent nature of water flowing out of culverts, we chose the Mask R-CNN model due to its robustness and better accuracy over other instance segmentation models.

Implementation

The Mask R-CNN model used in this study was downloaded as part of the TensorFlow Model Garden [67] and the TensorFlow Object Detection API [68]. These platforms provide models pre-trained on large datasets, such as ImageNet [69], therefore they include weights generalizable to most applications. However, the unoccupied area of the outlet is not a category included in any of the foundational object detection and classification datasets, therefore we needed to fine-tune the model using a dataset curated for that purpose.

The Mask R-CNN network is composed of the following components (Fig 2):

- Feature extractor network
- Region Proposal Network (RPN)
- Region of Interest alignment and aggregation (ROIAlign) layer
- Second-stage box and mask prediction network, comprising a Fast R-CNN object detector network along with a mask head.

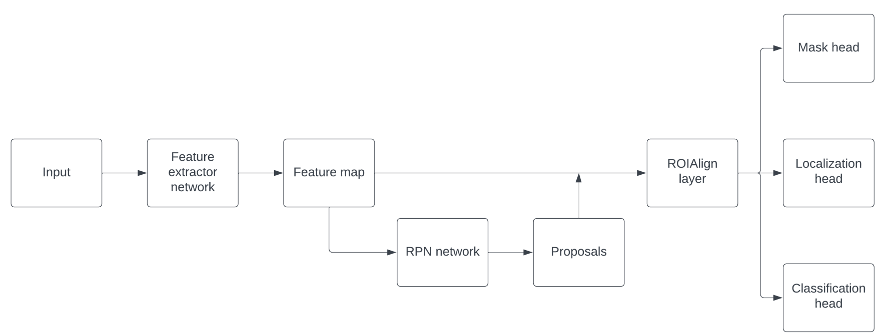

Fig 2. Mask R-CNN architecture scheme (reference: Sky Engine AI Developer Blog)

The feature extractor network is a deep neural network (DNN) that generates an abstraction of the input, called feature map, through a cascade of convolution and pooling operations. The initial layers of the feature extractor network handle low-level, general features, while the deeper layers address more high-level features due to the increased receptive field of these layers [70]. In this context, networks that are pre-trained on extensive datasets have developed a robust understanding of low-level features. Therefore, fine-tuning based on these features leads to more robust feature extraction, which in turn enhances the network's accuracy and convergence rate. This approach also saves time and computational resources compared to the random initialization of network weights.

Subsequently, deeper networks are more capable of developing contextual understanding, and thus better feature extraction, due to the wider receptive field they acquire in their later layers. However, this advantage comes at the cost of increased training and inference time. Therefore, there is a trade-off between speed and accuracy with respect to feature extractors: lighter networks, such as MobileNets [71], incur a lower computational burden and thus offer a higher processing rate. On the other hand, deeper networks like VGG16 [64] are better equipped to deliver richer features and, as a result, lead to higher accuracy. However, this comes with a reduction in processing rate and time. In this study, given the complexities of the scenes and the required precision, we opted for the Inception-ResNet-V2 [72] feature extractor which was shown to provide more robust features than lighter networks [73]. Apart from the network design and the geometric principles behind using feature extractors, the conversion of images into feature maps can also be viewed from a machine learning and optimization perspective. This is because they are taught to conform with the empirical risk relationship designated for the network, which is a significant aspect of DNNs and neural networks in general.

The network was configured to work with an input image size of 1024×1024 pixels. It was designed to detect and segment only one class of objects, which is the unoccupied area of the outlet. The network was trained using a batch size of 2 for 15 epochs, amounting to approximately 10,000 iterations. 'Batch size' refers to the number of inputs fed into the network during each iteration of network's weight optimization, and 'epoch' refers to the number of times the entire training dataset is used to train the model (optimizing the network weights). Also, the reason the training dataset is divided into batches during training is due to memory management considerations, as each input amounts to more than a million data points and, given the network's number of parameters, it incurs a high computational cost. In this study, due to the high resolution of the inputs and the limitations on the available graphics processing unit

(GPU), using batch sizes larger than 2 was not feasible and led to memory overflow.

During training, the empirical risk for each Region of Interest (ROI) is computed using the multi-task loss function [62]:

$$L = L_{cls} + L_{loc} + L_{mask} \tag{1}$$

where L represents the empirical risk or the total loss, L_{cls} represents the classification loss, L_{loc} represents the bounding box localization loss, and L_{mask} represents the mask loss, which characterizes instance segmentation accuracy. To compute the classification loss, the general method involves computing the output of the logistic regression, which in this case is done through the Softmax function, and then computing the loss using the cross-entropy loss function [65]:

$$L(p, u) = -\log p_u \tag{2}$$

$$p_u = \frac{e^{s_u}}{\sum_{i=0}^{k} e^{s_k}} \tag{3}$$

where, $L(p, u)$ represents the ROI classification loss, computed through the cross-entropy function, and p_u denotes the logistic regression value of the true class label, computed using the Softmax function. Also, s_u and s_k represent the outputs of the classification head's fully-connected layer for the true class label and for all the class labels, respectively.

The bounding box localization loss L_{loc} is also computed using the following equation [65]:

$$L_{loc} = \lambda_1 [u \geq 1] L_{loc}(t^u, v) \tag{4}$$

where λ_1 is the weight controlling the contribution of the localization loss to the overall loss, t^u represents the model's localization output for the true class label, v is the true localization label, and $[u \geq 1]$ is the indicator function, ensuring that only correct class detections contribute to the loss computation. In this study, the localization weight was set equal to 2.

The term $L_{loc}(t^u, v)$ is defined as the smooth L1 loss, given by::

$$L_{loc}(t^u, v) = \sum_{i \in x,y,w,h} \text{smooth}_{L_1}(t_i^u - v_i) \tag{5}$$

where t_i^u and v_i are respectively defined as $(t_x^u, t_y^u, t_w^u, t_h^u)$ and (v_x, v_y, v_w, v_h). Here, t_x and t_y represent scale-invariant shifts in x and y directions, respectively, and t_w and t_h denote the log-scale changes in the width and height of the bounding box. For example, the definition for t_x and t_w is as follows:

$$\begin{aligned} t_x &= (x_p - x_c)/w \\ t_w &= \log(w_p/w) \end{aligned} \tag{6}$$

Here, x_p and x_c respectively represent the predicted and the current x coordinates of the bounding box center. Similarly, w_p and w respectively denote the predicted and the current width of the bounding box. It should be noted that the network computes the entries of t_i and the predicted values are to be computed based on these entries.

In Eq (5), the smooth$_{L_1}$ function is also defined as follows [65]:

$$\text{Smooth}_{L_1}(x) = \begin{cases} 0.5 \times x^2 & \text{if} |x| < 1 \\ |x| - 0.5 & \text{otherwise} \end{cases} \tag{7}$$

Finally, to compute the mask loss L_{mask}, the Sigmoid function is applied to each pixel within the binary mask. Then, the binary cross-entropy loss for each pixel is computed, and the mask loss is calculated as the average of these pixel losses. Here, the Sigmoid function is defined as:

$$S(x) = \frac{1}{1 + e^{-x}} \tag{8}$$

where e is the Euler number.

Note that although the binary mask and the loss are initially computed for all classes, only the loss corresponding to the ground-truth class label is used for the mask loss term, and the losses for other classes are discarded [62]. In this study, the mask loss also had the biggest contribution to the total loss, with a weight set to 4.

The stochastic gradient descent (SGD) optimizer was used during training to fine-tune the initial weights. In addition, a cosine learning rate scheduler, with an initial learning rate of 0.008 and a 10% initial warm-up step, was employed to enhance the model's convergence during training. Here, the learning rate denotes to the step size the optimizer takes when moving toward a solution with minimum empirical risk. Regarding that, the learning rate is set higher during the initial steps of the optimization process, assuming the minimum is not very close to the current values, to expedite the search process given the first-order nature of the gradient descent method. Subsequently, the learning rate decreases through the rest of the steps until reaching a pre-defined final step size [74].

In addition to batch normalization [75], which is integrated into the network design to improve stability and convergence, two other regularization methods, namely L2 regularization and dropout [76], were also utilized. L2 regularization is a common technique used with iterative optimization approaches, like training machine learning and deep learning networks, to avoid overfitting. As a result, the model could generalize better to unseen data while it forces the model to take smaller weights. To implement this method, the term $\lambda \sum_i w_i^2$ is added to the network's loss function, where λ represents the regularization parameter and w_i the model weights. Dropout is also another technique that helps prevent overfitting. Applied to fully connected layers during training, it randomly deactivates a portion of neurons. This forces the model to rely less on individual neurons, thereby improving its robustness.

Dataset and training

The image dataset used to train the network was collected from three different sites in Raleigh, North Carolina (Fig 3). The dataset also includes images of a lab stormwater outlet prototype, as well as images downloaded through Google Images licensed under a Creative Commons (CC) agreement. For testing the network, images from a fourth site were used.

All images were taken using two brands of game cameras: HyperFire 2 Professional Covert IR Camera (RECONYX, Holmen, WI, USA) and A252 Trail Camera (Blazevideo, Kaysville, UT, USA). The RECONYX camera has a resolution of 2048×1440 and uses an IR sensor and IR illumination to provide high-quality night images. The Blazevideo camera has a resolution of 3840×2160 and uses a color night vision sensor. The images include day and night images, as well as images with and without flow. The flow images were taken during dark, rainy weather, i.e., prevalent conditions when stormwater flow occurs (Fig 3).

(a)

(b)

(c)

(d)

Fig 3. Representative sample images from various sites at North Carolina State University (NCSU) and surrounding areas: (a) Softball Field site; (b) Centennial Campus site; (c) Edward Mills Road site; (d) Motorpool site

To benchmark the performance of the Mask R-CNN model in correctly delineating the unoccupied area of the outlet within its inner edges, images from the Centennial Campus site (Fig 3b) were leveraged. However, given that this site wasn't capable of accommodating enough variety in flow, recordings from the Softball Field site (Fig 3a) were used to evaluate the approach's performance under field conditions. A chessboard calibration pattern was also installed coplanar with the culvert pipe outlet to establish the mapping between image coordinates (in pixels) and real-world coordinates (details below; Fig 4).

Table 1. Distribution of the images used for training the model

Google Image	Edward Mills Rd	Motorpool	Lab prototype	Softball	Total
11 (≈1%)	51 (≈4%)	104 (≈8%)	117 (≈9%)	1003 (≈80%)	1286 (100%)

Image annotations, i.e., manually delineating the empty area in culverts, with or without flow, were performed using the RectLabel annotation tool, which is exclusive to

(a) **(b)**

Fig 4. Representative images from the NC State University Softball site showing the chess board pattern panel installed above and to the left of the culvert: (a) daytime condition; (b) nighttime condition.

macOS operating system. The annotations were then exported and used in the Common Objects in Context (COCO) annotation standard [77]. The training dataset included around 1,300 annotated images, and the test dataset included around 700 images.

During training, to better represent real-world conditions, we randomly pre-processed the images with three effects. The first effect applied Gaussian noise to the images to simulate lower quality images. The second effect blended a white layer with the original image to simulate fog. The proportion of the white layer and the choice of image were both chosen randomly. The third effect added a changing number of blurred circles to the images to simulate droplets or fingerprints on the camera lens. These effects collectively helped to better represent what actually happens in the field and in practice. This was especially helpful given the relatively small number of training images, as it added more variety and therefore better prepare the network to deal with real-world scenarios.

For testing, due to the sequential correlation between the images and in an effort to create an inclusive, representative test dataset, the network was configured to randomly select 10% of the images for testing. Also, to better understand the model's performance on unseen data, the testing phase was conducted three times to mitigate the effects of random selection and ensure coverage of all situations encountered at the test site. Table 2 presents the results for the median case in the COCO metrics format [77].

Measurement methods

The water stage was calculated by the difference between the culvert diameter detected using the Mask R-CNN model and calculated via ellipse fitting (step 1), and the estimated distance between the top of the culvert and the water level detected using the model mask (step 2). The actual measurements expressed in real world units were performed thanks to fiducials (checkerboard) embedded in the images.

In step 1, we used our model to estimate the dimensions of a culvert outlet using images of an empty outlet captured over the period of a day. Since the outlet appears elliptical, its shape was estimated by fitting an ellipse to its inner edges. The measured major and minor axes of these fitted ellipses were then used as replicated estimates of the culvert diameter.

Ellipse fitting and measurements of an empty outlet

The dataset for this analysis includes 97 images from the Softball Field site taken during a full day at every 15 minutes (Fig 4)

To obtain measurements, the model first processes the image to extract a mask of the culvert. In the next step, the model identifies the contour of the mask within the binary image and fits an ellipse to this contour. This step was taken to simplify the subsequent steps based on the geometrical knowledge we have about culverts. In this process, drawing contours and fitting ellipses were performed through methods (functions) provided by the OpenCV package with the implementation details provided below [78].

Theoretically, since the model outputs a binary image for the object mask, drawing the contour involves calculating the gradients over the binary image and applying a threshold to isolate nonzero values. To fit an ellipse to the contour points, several approaches can be considered, depending on the characteristics of the contour points. In this study, given that the contour points closely align with the shape of an ellipse, a least-squares solution such as the LIN algorithm [79], which minimizes the algebraic distance between the points and the fitted ellipse, or the direct least squares ellipse fitting method [80] should provide a good approximation of the shape. Regarding that, given the general quadratic equation for the conic sections:

$$Ax^2 + Bxy + Cy^2 + Dx + Ey + F = 0 \tag{9}$$

Plugging points into the equation results in linear equations with respect to the parameters. Arranging these equations in a matrix format and imposing the constraint $||\bar{x}||^2 = 1$, where $\bar{x}$ represents the coefficients vector and the notation $||.||$ denotes the second norm of the vector, the constrained objective function can be written as:

$$E = ||\mathbf{A}\bar{x}|| - \lambda(||\bar{x}||^2 - 1) \tag{10}$$

Where λ is the Lagrange multiplier. To find the coefficients minimizing the objective function, we should take the gradient with respect to the coefficients vector and set it equal to zero. As a result, we'll get:

$$\nabla_{\mathbf{x}} E = \mathbf{A}^T\mathbf{A}\bar{x} - \lambda\bar{x} = 0 \tag{11}$$

To solve the above equation, we can use a method like the Singular Value Decomposition (SVD) method and the result would be the eigenvector corresponding to the least eigenvalue [79].

To compute the real-world measurements of the major and minor axes, the first step is to find the axes' endpoints. Since the ellipse's rotation angle equals the angle between its major axis and the vertical axis, as defined by OpenCV, we can easily compute the minor axis angle by adding $\pi/2$ radians to it, as the axes are perpendicular. Next, having the lengths of both axes, we can calculate the offsets of their endpoints from the ellipse center in the x and y directions using the following relations:

$$\begin{aligned} \Delta x &= L \times \cos\theta \\ \Delta y &= L \times \sin\theta \end{aligned} \tag{12}$$

Where L represents the length of the semi-major or semi-minor axis and θ represents their angle with the upward direction of the vertical axis. Finally, the end points coordinates in image system is computed as $[x_0 - \Delta x, y_0 - \Delta y]$ and $[x_0 + \Delta x, y_0 + \Delta y]$ where x_0 and y_0 represent the coordinates of the center of the ellipse.

We then compared these estimates with actual measurements taken in the field to assess the model's accuracy and performance. The time series nature of the image data allows us to assess the model's performance in two key areas: its adaptability to varying lighting conditions across the day and its robustness in maintaining consistent measurements over time.

Homography transformation to obtain real-world coordinates and measurements

The next step is to transform all values from pixels into a real-world coordinate system. For that, we employed a homography transformation, which is a linear transformation in projective space [81]. To obtain the homography matrix, an embedded 4×4 chessboard pattern with 9 inner points was used as the reference object (Fig 4), and the homography matrix was computed from these points based on the OpenCV package implementation [78].

To obtain real-world coordinates from image points, we first convert the coordinates from Euclidean to homogeneous form and arrange them as matrix columns. Next, we multiply the inverse homography matrix by these homogeneous image coordinates to obtain real-world coordinates in projective space. Since projective points are equivalent up to a scale factor, the resulting coordinates will also be determined up to scale. Finally, to recover Euclidean coordinates, we normalize each point by dividing its first two components by its third component (the homogeneous coordinate). The mathematical relationship between image points and their corresponding real-world coordinates under homography transformation can also be expressed as follows:

$$\begin{bmatrix} u \\ v \\ 1 \end{bmatrix} = H \begin{bmatrix} x \\ y \\ 1 \end{bmatrix} = \begin{bmatrix} h_{11} & h_{12} & h_{13} \\ h_{21} & h_{22} & h_{23} \\ h_{31} & h_{32} & h_{33} \end{bmatrix} \begin{bmatrix} x \\ y \\ 1 \end{bmatrix} \tag{13}$$

Water level measurements at culvert outlets

During flow events, water appears at the bottom of the culvert, leaving an unoccupied area above. Therefore, the full elliptic outline of the culvert does not appear in an image any longer. The Mask R-CNN model was employed to detect the unoccupied area of the outlet in an image or in each frame from a video. Subsequently, the homography transformation, based on the reference object in the image, was computed and applied to the pixels within the object mask to map them to the real-world coordinate system.

This transformation was also applied to an outline of the outlet extracted from a no-flow recording taken moments before the outflow began. Given that the fitted ellipse to the outlet mask determines the location of the center, the lengths of the axes, and the orientation of the ellipse in the image coordinate system, one can compute the coordinates for a representative number of points on the ellipse based on its parametric representation.

The parametric representation of an ellipse centered at $(0, 0)$ is given by:

$$\begin{aligned} x &= a \times \cos t \\ y &= b \times \sin t \end{aligned} \tag{14}$$

where the variables a and b are respectively the semi-major and semi-minor axes, and the variable t ranges from zero to 2π. In Euclidean 2D space, rotation is a linear transformation and can be applied through the following matrix multiplication:

$$\begin{pmatrix} x' \\ y' \end{pmatrix} = \begin{pmatrix} \cos\theta & -\sin\theta \\ \sin\theta & \cos\theta \end{pmatrix} \begin{pmatrix} x \\ y \end{pmatrix} \tag{15}$$

Assuming the ellipse orientation equal to θ, the parametric form of the ellipse will become:

$$\begin{aligned} x' &= x\cos\theta - y\sin\theta = a\cos t\cos\theta - b\sin t\sin\theta \\ y' &= x\sin\theta + y\cos\theta = a\cos t\sin\theta + b\sin t\cos\theta \end{aligned} \tag{16}$$

Finally, assuming the center of the ellipse is at (x_0, y_0), the parametric representation of the ellipse becomes:

$$\begin{aligned} x &= x_0 + a\cos t\cos\theta - b\sin t\sin\theta \\ y &= y_0 + a\cos t\sin\theta + b\sin t\cos\theta \end{aligned} \tag{17}$$

To generate points on the ellipse, one should divide the range of the variable t into the desired number of values and plug them into Eq (17). The generated points can then be mapped to their real-world coordinates using the homography transformation obtained in the previous steps. Having the ellipse points in their real-world coordinates, the height is calculated as the absolute difference between the maximum and minimum y-coordinates of the points. Note that this step is necessary because the fitted ellipse's major and minor axes may not be aligned with the vertical axis, leading to the height being a value between these two axes.

Performance assessment

Outlet diameter

We used our approach to estimate the dimensions of a culvert outlet using images of an empty outlet captured over the period of a day. Since the outlet appears elliptical, its shape was estimated by fitting an ellipse to its inner edges. The measured major and minor axes of these fitted ellipses were then used to compare between instances. The axes lengths gave two largely independent measurements of the same distances, i.e., the culvert diameter. We then compared these estimates to actual measurements taken in the field to assess the model's accuracy and performance. The time series nature of the image data allows us to assess the model's performance in two key areas: its adaptability to varying lighting conditions across the day and its robustness in maintaining consistent measurements over time.

Water depth

To assess the performance of the model, an initial attempt was made to use measurements from a Sontek IQ (Xylem, Washington, D.C., USA) flowmeter mounted inside the culvert. However, this method did not yield robust results due to the highly turbulent conditions and highly variable water level in the culvert (e.g., $\pm$ 5 cm in 1 sec), which the sensor was not able to capture. Furthermore, the flowmeter's mechanism required about 10 cm of water level above the sensor to start recording values, a condition not met in many cases considered in this study. Using a staff gauge, typically employed in stream water level monitoring, was also impractical due to the area's dimensional constraints and the turbulent condition of the water in the culvert. Therefore, the only viable option was to visually verify the water level in each frame. To facilitate this, and assuming the coplanarity between the checkerboard and the plane of the culvert face, a series of horizontal perspective lines were drawn as a guide to help the observer make an educated and potentially accurate judgment.

To draw the perspective lines around the object mask, we first map the mask points to their real-world coordinates and extract the range of values in each direction. Allowing for a leeway around the mask edges, the horizontal perspective lines span between the maximum and minimum x-coordinates in the real-world system. By converting both ends of the lines from the real-world coordinate system to the image coordinate system using the inverse of the homography transformation, the lines are obtained and can then be drawn on the image. Additionally, to aid in the visual reading of the water level, the levels corresponding to the midpoint and the top point of the mask were highlighted with blue lines. Furthermore, counting lines from the midpoint level, every fifth line was marked with a red color for better differentiation. A view of the outcome of these processes is shown in Fig 5.

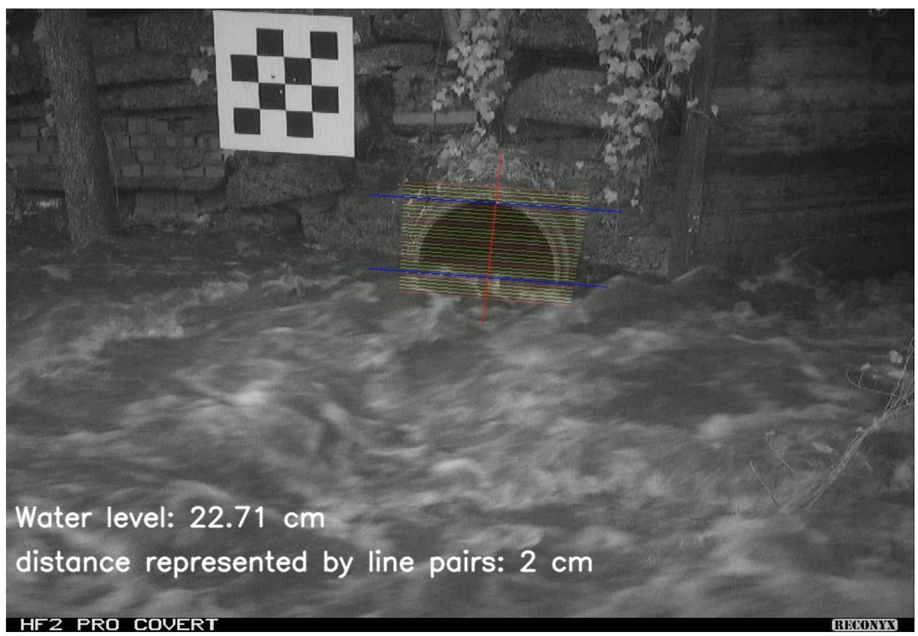

Fig 5. Horizontal perspective lines over the unoccupied area facilitating visual observation

In the processing pipeline, each frame is treated independently to avoid the resonance effect of errors across different frames. Accordingly, the homography transformation, as well as the mapping between the image coordinate system and the real-world coordinate system, is performed for each frame for both the object mask and the culvert's fitted ellipse.

Results and Discussion

Segmentation model performance

Since our approach integrates two components — a deep learning model for detecting unoccupied culvert areas and geometric transformations for real-world coordinate mapping — its evaluation could be considered from both algorithmic detection accuracy and geometric measurement precision perspectives. Following standard practices in deep learning evaluation, we assessed the Mask R-CNN model's detection accuracy using COCO evaluation metrics, including average precision (AP) and average recall (AR).

These metrics are standard to object detection and instance segmentation tasks evaluations, and are widely used by practitioners in the field to report their models' results. In this context, precision and recall are defined as follows:

$$\begin{aligned} \text{Precision} &= \frac{TP}{TP+FP} \\ \text{Recall (Sensitivity)} &= \frac{TP}{TP+FN} \end{aligned} \tag{18}$$

Where TP indicates true positive detections, FN denotes false negative detections, and FP is for false positive detections. As a result, the denominator of the recall formula corresponds to the actual positive cases, while the denominator of the precision formula represents all positive detections, irrespective of whether they are true or false.

Table 2 presents the model's AP and AR metrics evaluated at different Intersection over Union (IoU) thresholds. The AP reported in the table is computed by taking the mean of precision values at different recall levels, i.e., the area under the precision-recall curve. AR is also computed by taking the mean of recall values. Finally, the IoU is defined as the ratio of the intersection between the ground-truth label and the segmentation mask to their union.

Model performance in measuring outlet diameter

Results of the culvert diameter measurements in the field are reported in Fig 6, expressed in pixel coordinates (Fig 6a and Fig 6b) and in real world coordinates (Fig 6c and Fig 6d). The scatter plots in Fig 6c and Fig 6d show that the size in pixels for the minor axis is about 7% smaller than the major axis. This is expected as there was an

Table 2. Model evaluation report on the test dataset using COCO metrics. Performance is reported for three object size categories, considering the maximum number of detections (maxDet) and the corresponding IoU threshold or range.

Average Precision (AP)	@ IoU=0.50:0.95	area=all	maxDets=100	0.841
Average Precision (AP)	@ IoU=0.50	area=all	maxDets=100	1.000
Average Precision (AP)	@ IoU=0.75	area=all	maxDets=100	0.981
Average Precision (AP)	@ IoU=0.50:0.95	area=small	maxDets=100	-1.000
Average Precision (AP)	@ IoU=0.50:0.95	area=medium	maxDets=100	-1.000
Average Precision (AP)	@ IoU=0.50:0.95	area=large	maxDets=100	0.841
Average Precision (AP)	@ IoU=0.50:0.95	area=all	maxDets=1	0.885
Average Recall (AR)	@ IoU=0.50:0.95	area=all	maxDets=10	0.886
Average Recall (AR)	@ IoU=0.50:0.95	area=all	maxDets=100	0.886
Average Recall (AR)	@ IoU=0.50:0.95	area=small	maxDets=100	-1.000
Average Recall (AR)	@ IoU=0.50:0.95	area=medium	maxDets=100	-1.000
Average Recall (AR)	@ IoU=0.50:0.95	area=large	maxDets=100	0.886

angle between the camera axis and the culvert centerline, and that the culvert mouth appeared as an ellipse on images. Upon perspective correction, the ellipse should theoretically be converted back to a circle, and the major and minor axes should have about the same dimensions.

The model shows consistency in its measurements throughout the day, under varying lighting and environmental conditions. The model detected an outlier, clearly recognizable in Fig 6d, which corresponds to the reflection of the culvert in the nearby pond (Fig 7).

Fig 8 illustrates the errors in the axes measurements. Based on this, we can observe that the majority of the major axis measurements tend to underestimate the size of the diameter between zero and 1.5 centimeters, while the minor axis measurements appear less biased, mostly having an absolute error value of less than 0.5 centimeters. Note that for better visualization in the boxplots, the single outlier mentioned earlier was removed.

Upon closer examination of Fig 6a and Fig 6b, one can see that the detection patterns differ between day and night. To further investigate this difference visually, the range of measurements for the major and minor axes during daytime and nighttime are illustrated in Fig 9. Based on the plots, although the extent of the measured values'

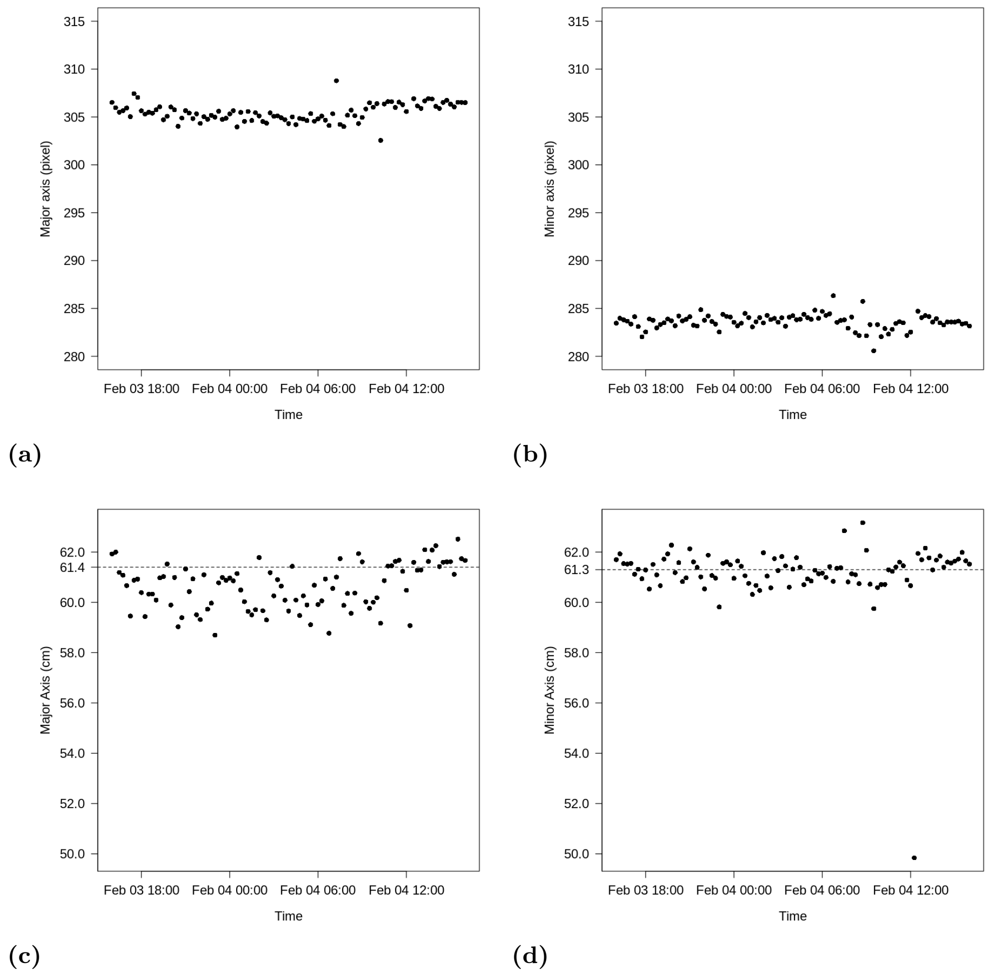

Fig 6. Major and minor axis lengths in the image coordinate system (a and b) and the real-world coordinate system (c and d). Each point represents an image captured every 15 minutes in February 2024 from an empty culvert at the Softball site.

range is nearly the same, a pattern of underestimation is evident in night images, especially pronounced for the major axis measurement. This is possibly due to the lack of light and/or uneven distribution of the camera's IR flash over the culvert edges.

Fig 6c and Fig 6d reveal an underestimation pattern in the fitted ellipse's major axis measurements, while the minor axis measurements cluster around the actual value. Several factors could contribute to this discrepancy.

One factor could be the effect of lighting conditions on the model's detections. Although the model maintains reasonable accuracy throughout the day, Fig 9 shows that major axis measurements made during daytime are centered around the actual diameter value (difference between median and the actual value < 1 mm) while the

Fig 7. An example of a false positive detection: the model identified both a culvert and its reflection in a pond.

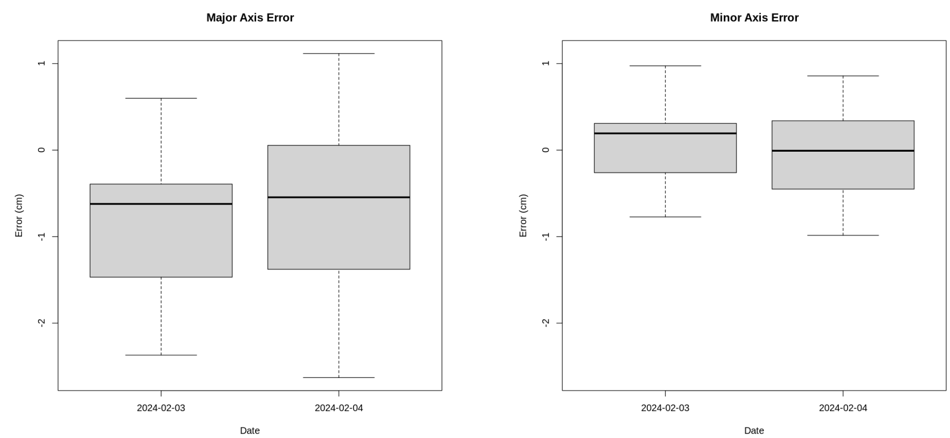

(a) **(b)**

Fig 8. Boxplots of errors in real-world axis measurements: major axis (a) and minor axis (b)

measurements at night are underestimated (median value 1 cm lower than actual one). Another contributing factor could be the presence of intermittent environmental effects, such as shadows caused by vegetation in the surroundings and changes in sunlight angle and direction, as well as reflections from water. These factors can either mislead the model to detect the reflection of the culvert instead of the culvert itself, as happened in one instance, or alter the light pattern over the culvert, thereby deviating the model

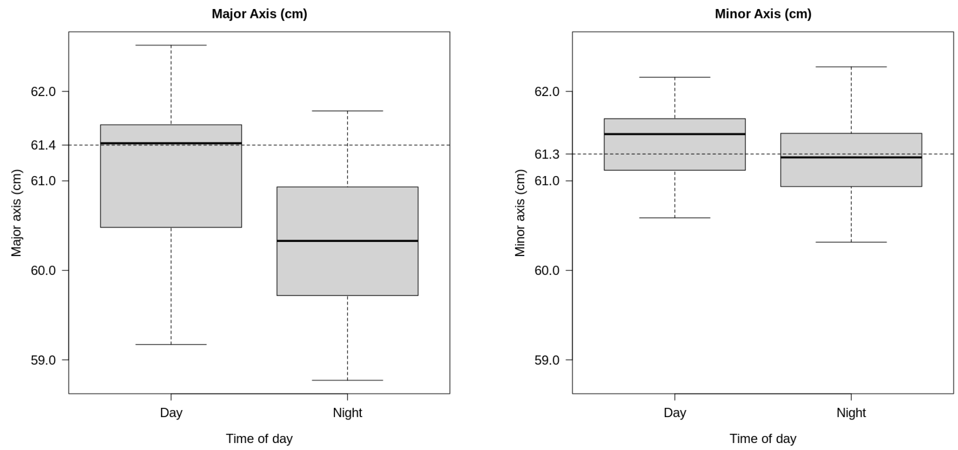

(a) (b)

Fig 9. Boxplots of real-world measurements for the major and minor axes during day and night

from more accurate detection by providing false contrast around the culvert.

It is interesting to observe that the dimensions of the minor axis are not as sensitive to these factors as those of the major axis and are scattered around the reference values within approximately $\pm$ 1 cm.

Camera settings could also play a role, though not evident from the analysis. Every lens system has a degree of distortion, including radial and tangential. While tangential distortion, which displaces points perpendicular to the radial direction from the camera's optical center, is often negligible, radial distortion, including barrel and pincushion distortions, which moves points respectively closer or farther from the optical center along a radial direction, is not typically negligible and should be considered [82].

As illustrated in Fig 4, although the culvert is located near the center of the image, limiting the effect of radial distortion on its representation, the presence of the chessboard near the image borders indicates a situation where radial distortion could have a significant effect. This distortion affects the accurate detection of inner points used during homography estimation, which could then translate into errors in the real-world measurements of the outlet area.

This highlights the importance of locating the reference object near the outlet. While mounting the chessboard farther from the outlet makes it harder to align with the culvert's face, it also amplifies the effect of radial distortion, leading to more significant errors in culvert area measurements. Additionally, having the outlet farther away amplifies any errors introduced by incorrect measurements of the reference points, as these errors get magnified with distance. Nevertheless, it is important to acknowledge the limitations imposed by field conditions, where ideal scenarios are not always achievable.

In addition to the factors mentioned above, other factors like misalignment between the chessboard and the outlet, caused by natural factors such as heavy rain, creep of the reference object's connection, and animal interference with the reference object, could contribute to errors. However, measuring the effect of these factors requires regular field inspections, as well as more advanced laboratory and numerical analyses.

Model performance in water level measurement at the outlet

To evaluate the proposed approach for water level measurement, two real-world conditions were considered. First, to assess performance under turbulent conditions, common in stormwater system outflows, we used footage from a turbulent outlet. Second, we evaluated performance using footage of relatively calm outflow and compared the results.

Fig 10a illustrates the time series of the proposed approach's measurements alongside corresponding manual readings for the turbulent condition. As shown, at this particular site (Softball field site on NC State University main campus), stormflow was extremely turbulent, with water levels fluctuating by more than 10 cm within 5 seconds, as evidenced by manual readings. This degree of rapid fluctuation would be difficult to capture accurately using other sensors or instruments, such as those without stilling wells.

Based on Fig 10a, it is also observable that the model's estimations closely track visual measurements of the water stage. However, the model tends to overestimate the water stage in most cases. The general overestimation of the Mask R-CNN model's predictions compared to the visual measurements is illustrated in Fig 11a, expressed as the centimeter difference between the two. Based on the plot, 75% of the measurements were overestimated by 0.4 to 1.2 cm. Comparing the water level estimation error range in Fig 11a with the error range observed for the major and minor axes measurements in Fig 8, we see that the model exhibits a consistent pattern of forming the mask slightly

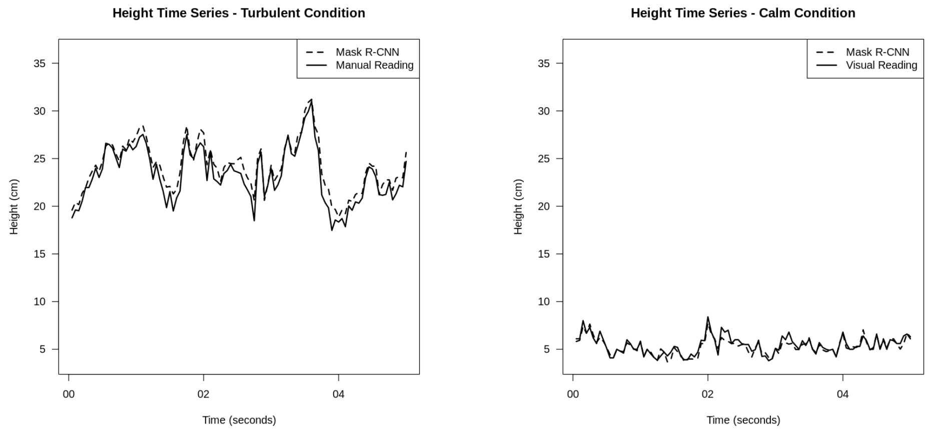

(a) **(b)**

Fig 10. Comparison of model-derived and visually observed water levels at the outlet for (a) turbulent and (b) calm flow conditions

before the actual surface in both scenarios. This is manifested as a negative error in the first method, as shown in Fig 8, and an overestimation of the water level during the event shown in Fig 11a.

Fig 10b shows the model-predicted and visually observed water stage time series for the calm condition. Compared to the turbulent condition (Fig 10a), the range of water level fluctuations decreased to approximately 4 cm, less than half the range observed under turbulent conditions. Subsequently, the error range (Fig 11b) is also noticeably smaller and centered around zero, indicating less pronounced overestimation. However, the positive skew of the boxplot suggests some overestimation persists.

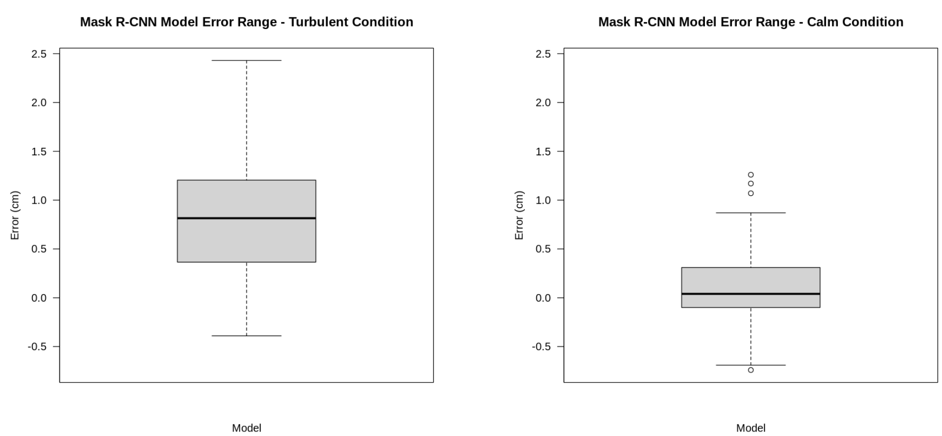

(a) **(b)**

Fig 11. Boxplots of model error relative to visual water stage measurements under (a) turbulent and (b) calm flow conditions

The results demonstrate the robustness of the proposed approach in tracking water level fluctuations across different flow regimes. While increased turbulence has the potential to introduce greater error, the approach exhibited satisfactory performance even under highly turbulent conditions, as detailed in the turbulent flow analysis.

Conclusion

In this study, we report a proof of concept for a computer vision and machine learning (CV-ML) approach based on the Mask R-CNN architecture to measure water level at the outlets of stormwater culverts, from which one could calculate the discharge (error on discharge not part of this article). The ML model shows that it is able to satisfactorily detect the empty and flowing outlets from busy images with variable lighting conditions, including day and night. To evaluate the approach's performance in real-world conditions in the field, two complementary methods were defined. In the first method, the approach's performance was tested from its ability to measure stormwater culvert's diameter during no flow from images taken during a day period in the field. In the second method, its performance was evaluated on actual water levels measured during turbulent and calm flow events. The results demonstrate satisfactory performance, particularly considering the complexity of the conditions, with a maximum overestimation in water stage of 0.8 ± 0.4 cm. These promising results demonstrate the potential of camera-based systems combined with machine learning to measure water stage in stormwater outflows, offering a viable alternative in many instances.

References

1. Tsihrintzis VA, Hamid R. Modeling and Management of Urban Stormwater Runoff Quality: A Review. Water Resour Manage. 1997;11:137–164.

2. Us Epa O. Urbanization - Stormwater Runoff. 2015;.

3. Winston R J , Hunt W F . Characterizing Runoff from Roads: Particle Size Distributions, Nutrients, and Gross Solids. J Environ Eng. 2017;143(1):04016074. doi:10.1061/(ASCE)EE.1943-7870.0001148.

4. Müller A, Österlund H, Marsalek J, Viklander M. The pollution conveyed by urban runoff: A review of sources. Sci Total Environ. 2020;709:136125. doi:10.1016/j.scitotenv.2019.136125.

5. Kriech AJ, Osborn LV. Review of the impact of stormwater and leaching from pavements on the environment. J Environ Manage. 2022;319:115687. doi:10.1016/j.jenvman.2022.115687.

6. Prudencio L, Null SE. Stormwater management and ecosystem services: a review. Environ Res Lett. 2018;13(3):033002. doi:10.1088/1748-9326/aaa81a.

7. Chakravarthy S, Sharma R, Kasturi R. Noncontact level sensing technique using computer vision. IEEE Trans Instrum Meas. 2002;51(2):353–361.

8. Kaplan NH, Sohrt E, Blume T, Weiler M. Monitoring ephemeral, intermittent and perennial streamflow: a dataset from 182 sites in the Attert catchment, Luxembourg. Earth System Science Data. 2019;11(3):1363–1374.

9. Lin YT, Lin YC, Han JY. Automatic water-level detection using single-camera images with varied poses. Measurement. 2018;127:167–174. doi:https://doi.org/10.1016/j.measurement.2018.05.100.

10. Noto S, Tauro F, Petroselli A, Apollonio C, Botter G, Grimaldi S. Low-cost stage-camera system for continuous water-level monitoring in ephemeral streams. Hydrol Sci J. 2022;67(9):1439–1448.

11. Schoener Gerhard. Time-Lapse Photography: Low-Cost, Low-Tech Alternative for Monitoring Flow Depth. J Hydrol Eng. 2018;23(2):06017007.

12. Takagi Y, Tsujikawa A, Takato M, Saito T, Kaida M. Development of a noncontact liquid level measuring system using image processing. Water Sci Technol. 1998;37(12):381–387.

13. Jeanbourquin D, Sage D, Nguyen L, Schaeli B, Kayal S, Barry DA, et al. Flow measurements in sewers based on image analysis: automatic flow velocity algorithm. Water Sci Technol. 2011;64(5):1108–1114.

14. Jodeau M, Hauet A, Paquier A, Le Coz J, Dramais G. Application and evaluation of LS-PIV technique for the monitoring of river surface velocities in high flow conditions. Flow Meas Instrum. 2008;19(2):117–127.

15. Kantoush SA, Schleiss AJ, Sumi T, Murasaki M. LSPIV implementation for environmental flow in various laboratory and field cases. Journal of Hydro-environment Research. 2011;5(4):263–276.

16. Fujita I, Muste M, Kruger A. Large-scale particle image velocimetry for flow analysis in hydraulic engineering applications. J Hydraul Res. 1998;36(3):397–414.

17. Wu H, Zhao R, Gan X, Ma X. Measuring Surface Velocity of Water Flow by Dense Optical Flow Method. Water. 2019;11(11):2320.

18. Kim J, Kim J. Estimation of Water Surface Flow Velocity in Coastal Video Imagery by Visual Tracking with Deep Learning. J Coast Res. 2020;.

19. Fujita I, Notoya Y, Tani K, Tateguchi S. Efficient and accurate estimation of water surface velocity in STIV. Environ Fluid Mech. 2019;19(5):1363–1378.

20. Engelen L, Creëlle S, Schindfessel L, De Mulder T. Spatio-temporal image-based parametric water surface reconstruction: a novel methodology based on refraction. Meas Sci Technol. 2018;29(3):035302.

21. Holland KT, Puleo JA, Kooney TN. Quantification of swash flows using video-based particle image velocimetry. Coast Eng. 2001;44(2):65–77.

22. Bradley AA, Kruger A, Meselhe EA, Muste MVI. Flow measurement in streams using video imagery. Water Resour Res. 2002;38(12):51–1–51–8.

23. Creutin JD, Muste M, Bradley AA, Kim SC, Kruger A. River gauging using PIV techniques: a proof of concept experiment on the Iowa River. J Hydrol. 2003;277(3):182–194.

24. Hauet A, Creutin JD, Belleudy P. Sensitivity study of large-scale particle image velocimetry measurement of river discharge using numerical simulation. J Hydrol. 2008;349(1):178–190.

25. Muste M, Fujita I, Hauet A. Large-scale particle image velocimetry for measurements in riverine environments. Water Resour Res. 2008;44(4).

26. USGS. Hydrologic Imagery Visualization and Information System (HIVIS); 2022. https://www.usgs.gov/tools/hydrologic-imagery-visualization-and-information-system-hivis. Available from: https://www.usgs.gov/tools/hydrologic-imagery-visualization-and-information-system-hivis.

27. Birgand F, Chapman K, Hazra A, Gilmore T, Etheridge R, Staicu AM. Field performance of the GaugeCam image-based water level measurement system. PLOS Water. 2022;1(7):e0000032.

28. Hauet Alexandre, Kruger Anton, Krajewski Witold F , Bradley Allen, Muste Marian, Creutin Jean-Dominique, et al. Experimental System for Real-Time Discharge Estimation Using an Image-Based Method. J Hydrol Eng. 2008;13(2):105–110.

29. Le Coz J, Hauet A, Pierrefeu G, Dramais G, Camenen B. Performance of image-based velocimetry (LSPIV) applied to flash-flood discharge measurements in Mediterranean rivers. J Hydrol. 2010;394(1):42–52.

30. Peña-Haro S, Carrel M, Lüthi B, Hansen I, Lukes R. Robust Image-Based Streamflow Measurements for Real-Time Continuous Monitoring. Frontiers in Water. 2021;3.

31. Le Coz J, Renard B, Vansuyt V, Jodeau M, Hauet A. Estimating the uncertainty of video-based flow velocity and discharge measurements due to the conversion of field to image coordinates. Hydrol Process. 2021;35(5).

32. Chahrour N, Castaings W, Barthélemy E. Image-based river discharge estimation by merging heterogeneous data with information entropy theory. Flow Meas Instrum. 2021;81:102039.

33. Tsubaki R, Fujita I, Tsutsumi S. Measurement of the flood discharge of a small-sized river using an existing digital video recording system. Journal of Hydro-environment Research. 2011;5(4):313–321.

34. Bechle Adam J , Wu Chin H , Liu Wen-Cheng, Kimura Nobuaki. Development and Application of an Automated River-Estuary Discharge Imaging System. J Hydraul Eng. 2012;138(4):327–339.

35. Ji HW, Yoo SS, Lee BJ, Koo DD, Kang JH. Measurement of Wastewater Discharge in Sewer Pipes Using Image Analysis. Water. 2020;12(6):1771.

36. Zhao H, Chen H, Liu B, Liu W, Xu CY, Guo S, et al. An improvement of the Space-Time Image Velocimetry combined with a new denoising method for estimating river discharge. Flow Meas Instrum. 2021;77:101864.

37. Chapman KW, Gilmore TE, Chapman CD, Birgand F, Mittlestet AR, Harner MJ, et al. Technical note: Openâsource software for waterâlevel measurement in images with a calibration target. Water Resour Res. 2022;58(8).

38. Zhang Z, Zhou Y, Liu H, Gao H. In-situ water level measurement using NIR-imaging video camera. Flow Meas Instrum. 2019;67:95–106.

39. Eltner A, Bressan PO, Akiyama T, Gonçalves WN, Marcato Junior J. Using deep learning for automatic water stage measurements. Water Resour Res. 2021;57(3).

40. Pan J, Yin Y, Xiong J, Luo W, Gui G, Sari H. Deep Learning-Based Unmanned Surveillance Systems for Observing Water Levels. IEEE Access. 2018;6:73561–73571.

41. Yu J, Hahn H. Remote Detection and Monitoring of a Water Level Using Narrow Band Channel. J Inf Sci Eng. 2010;26(1):71–82.

42. Fujita I, Watanabe H, Tsubaki R. Development of a nonâintrusive and efficient flow monitoring technique: The spaceâtime image velocimetry (STIV). International Journal of River Basin Management. 2007;5(2):105–114.

43. Iwahashi M, Udomsiri S. Water Level Detection from Video with Fir Filtering. In: 2007 16th International Conference on Computer Communications and Networks; 2007. p. 826–831.

44. Kim Y, Muste M, Hauet A, Krajewski WF, Kruger A, Bradley A. Stream discharge using mobile large-scale particle image velocimetry: A proof of concept.

Water Resources Research. 2008;44(9). doi:https://doi.org/10.1029/2006WR005441.

45. Iwahashi M, Udomsiri S, Imai Y, Muramatsu S. Water Level Detection for Functionally Layered Video Coding. In: 2007 IEEE International Conference on Image Processing. vol. 2; 2007. p. II – 321–II – 324.

46. Gilmore TE, Birgand F, Chapman KW. Source and magnitude of error in an inexpensive image-based water level measurement system. J Hydrol. 2013;496:178–186.

47. Nguyen LS, Schaeli B, Sage D, Kayal S, Jeanbourquin D, Barry DA, et al. Vision-based system for the control and measurement of wastewater flow rate in sewer systems. Water Sci Technol. 2009;60(9):2281–2289.

48. Kim J, Han Y, Hahn H. Embedded implementation of image-based water-level measurement system. IET Comput Vision. 2011;5(2):125–133.

49. Hies T, Parasuraman SB, Wang Y, Duester R, Eikaas H, Tan K. Enhanced water-level detection by image processing.; 2012.

50. Zhang Z, Zhou Y, Liu H, Zhang L, Wang H. Visual Measurement of Water Level under Complex Illumination Conditions. Sensors. 2019;19(19).

51. Hansen I, Warriar R, Satzger C, Sattler M, Luethi B, Peña-Haro S, et al. An innovative image processing method for flow measurement in open channels and rivers. In: Global Conference & Exhibition-2017 "Innovative Solutions in Flow Measurement and Control-Oil, Water and Gas; 2017. p. 28–30.

52. Birgand F, Lellouche G, Appelboom TW. Measuring flow in non-ideal conditions for short-term projects: Uncertainties associated with the use of stage-discharge rating curves. J Hydrol. 2013;503:186–195. doi:10.1016/j.jhydrol.2013.09.007.

53. Horn BKP, Schunck BG. Determining Optical Flow. Artif Intell. 1981;17:185–203.

54. Huang YW, Chen CY, Tsai CH, Shen CF, Chen LG. Survey on Block Matching Motion Estimation Algorithms and Architectures with New Results. J VLSI Signal Process Syst Signal Image Video Technol. 2006;42(3):297–320.

55. Keane RD, Adrian RJ. Theory of cross-correlation analysis of PIV images. Appl Sci Res. 1992;49(3):191–215.

56. Jähne B. Spatio-temporal image processing: theory and scientific applications. Springer; 1993.

57. Willert CE, Gharib M. Digital particle image velocimetry. Exp Fluids. 1991;10(4):181–193.

58. Lloyd PM, Stansby PK, Ball DJ. Unsteady surface-velocity field measurement using particle tracking velocimetry. J Hydraul Res. 1995;33(4):519–534.

59. Gupta A, Chang T, Walker J, Letcher B. Towards Continuous Streamflow Monitoring with Time-Lapse Cameras and Deep Learning. In: ACM SIGCAS/SIGCHI Conference on Computing and Sustainable Societies (COMPASS). COMPASS '22. New York, NY, USA: Association for Computing Machinery; 2022. p. 353–363.

60. Haurum JB, Bahnsen CH, Pedersen M, Moeslund TB. Water Level Estimation in Sewer Pipes Using Deep Convolutional Neural Networks. Water. 2020;12(12):3412.

61. Young SN, Han M, Peschel JM. Computer vision approach for tile drain Outflow rate estimation. Appl Eng Agric. 2023;39(2):153–165. doi:10.13031/aea.15157.

62. He K, Gkioxari G, Dollár P, Girshick R. Mask R-CNN. In: 2017 IEEE International Conference on Computer Vision (ICCV). IEEE; 2017. p. 2980–2988.

63. Girshick R, Donahue J, Darrell T, Malik J. Rich Feature Hierarchies for Accurate Object Detection and Semantic Segmentation. In: 2014 IEEE Conference on Computer Vision and Pattern Recognition; 2014. p. 580–587.

64. Simonyan K, Zisserman A. Very Deep Convolutional Networks for Large-Scale Image Recognition. arXiv e-prints. 2014; p. arXiv:1409.1556. doi:10.48550/arXiv.1409.1556.

65. Girshick R. Fast R-CNN. In: 2015 IEEE International Conference on Computer Vision (ICCV); 2015. p. 1440–1448.

66. Ren S, He K, Girshick R, Sun J. Faster R-CNN: Towards Real-Time Object Detection with Region Proposal Networks. IEEE Trans Pattern Anal Mach Intell. 2017;39(6):1137–1149.

67. Yu H, Chen C, Du X, Li Y, Rashwan A, Hou L, et al.. TensorFlow Model Garden; 2020.

68. Huang J, Rathod V, Sun C, Zhu M, Korattikara A, Fathi A, et al. Speed/Accuracy Trade-Offs for Modern Convolutional Object Detectors. In: 2017 IEEE Conference on Computer Vision and Pattern Recognition (CVPR); 2017. p. 3296–3297.

69. Deng J, Dong W, Socher R, Li LJ, Li K, Fei-Fei L. ImageNet: A large-scale hierarchical image database. In: 2009 IEEE Conference on Computer Vision and Pattern Recognition; 2009. p. 248–255.

70. Redmon J, Divvala S, Girshick R, Farhadi A. You Only Look Once: Unified, Real-Time Object Detection. In: 2016 IEEE Conference on Computer Vision and Pattern Recognition (CVPR); 2016. p. 779–788.

71. Howard AG, Zhu M, Chen B, Kalenichenko D, Wang W, Weyand T, et al. MobileNets: Efficient Convolutional Neural Networks for Mobile Vision Applications. arXivorg. 2017;.

72. Szegedy C, Ioffe S, Vanhoucke V, Alemi A. Inception-v4, Inception-ResNet and the Impact of Residual Connections on Learning. arXivorg. 2016;.

73. Zhang Z, Wang Y, Zhang J, Mu X. Comparison of multiple feature extractors on Faster RCNN for breast tumor detection. In: 2019 8th International Symposium on Next Generation Electronics (ISNE); 2019. p. 1–4.

74. Loshchilov I, Hutter F. SGDR: Stochastic Gradient Descent with Warm Restarts. arXivorg. 2016;.

75. Ioffe S, Szegedy C. Batch Normalization: Accelerating Deep Network Training by Reducing Internal Covariate Shift. arXivorg. 2015;.

76. Srivastava N, Hinton G, Krizhevsky A, Sutskever I, Salakhutdinov R. Dropout: A Simple Way to Prevent Neural Networks from Overfitting. J Mach Learn Res. 2014;15:1929–1958.

77. Lin TY, Maire M, Belongie S, Hays J, Perona P, Ramanan D, et al. Microsoft COCO: Common Objects in Context. In: Fleet D, Pajdla T, Schiele B, Tuytelaars T, editors. Computer Vision – ECCV 2014. Cham: Springer International Publishing; 2014. p. 740–755.

78. Bradski G. The OpenCV Library. Dr Dobb's j softw tools prof program. 2000;.

79. Fitzgibbon AW, Fisher RB. A buyer's guide to conic fitting. In: Proceedings of the 6th British Conference on Machine Vision (Vol. 2). BMVC '95. GBR: BMVA Press; 1995. p. 513–522.

80. Fitzgibbon A, Pilu M, Fisher RB. Direct least square fitting of ellipses. IEEE Trans Pattern Anal Mach Intell. 1999;21(5):476–480.

81. Hartley R, Zisserman A. Multiple View Geometry in Computer Vision. Cambridge University Press; 2004.

82. Tomasi C. In: A Simple Camera Model; 2017.